

Crossover between short and long range proximity effects in SFS junctions with Ni-based ferromagnets.

O. M. Kapran¹, T. Golod¹, A. Iovan^{1,2}, A. S. Sidorenko^{3,4}, A. A. Golubov^{5,6} and V. M. Krasnov^{1,6*}

¹ Department of Physics, Stockholm University, AlbaNova University Center, SE-10691 Stockholm, Sweden;

² Department of Applied Physics, Royal Institute of Technology, SE-10691 Stockholm, Sweden;

³ Institute of Electronic Engineering and Nanotechnologies ASM, MD2028 Kishinev, Moldova;

⁴ I.S. Turgenyev Orel State University, 302026 Orel, Russia;

⁵ Faculty of Science and Technology and MESA+ Institute of Nanotechnology, University of Twente 7500 AE, Enschede, The Netherlands; and

⁶ Moscow Institute of Physics and Technology, State University, 141700 Dolgoprudny, Russia.

We study Superconductor/Ferromagnet/Superconductor junctions with CuNi, PtNi, or Ni interlayers. Remarkably, we observe that supercurrents through Ni can be significantly larger than through diluted alloys. The phenomenon is attributed to the dirtiness of disordered alloys leading to a short coherence length despite a small exchange energy. To the contrary, pure Ni is clean resulting in a coherence length as long as in a normal metal. Analysis of temperature dependencies of critical currents reveals a crossover from short (dirty) to long (clean) range proximity effects in $\text{Pt}_{1-x}\text{Ni}_x$ with increasing Ni concentration. Our results point out that structural properties of a ferromagnet play a crucial role for the proximity effect and indicate that conventional strong-but-clean ferromagnets can be advantageously used in superconducting spintronic devices.

I. INTRODUCTION

A competition between superconductivity and ferromagnetism leads to an unconventional proximity effect, studied both theoretically [1–18] and experimentally [19–41]. In strong ferromagnets (F) Fe, Co, Ni, exchange energies, $E_{ex} \sim 1000$ K, are much larger than the energy gap, $\Delta \sim 1 - 10$ K, in low- T_c superconductors (S). Therefore, spin-singlet Cooper pairs are usually broken at a very short range ~ 1 nm in F, as shown by many experimental works [21, 26–28, 31, 34, 39, 40]. There are, however, reports about a long range proximity effect (LRPE) (tens to hundreds of nm) [19, 25, 30, 33, 35], which is often ascribed to the spin-triplet order parameter that should be immune to the ferromagnetic order.

Interpretation of LRPE remains controversial. First, there is a seeming irreproducibility of experimental results, cf. Refs. [19, 30, 35] and [21, 40]. Second, the triplet order should appear only in the noncollinear magnetic state [6, 7, 11], the origin of which is often unclear for structures containing only one F layer. Although several subtle effects, such as quantum fluctuations [3], active interfaces [5], domains [28, 38], inhomogeneities [10, 13, 17] and spin-orbit coupling [16, 17] were suggested, they are difficult to confirm or control in experiment. Finally, the proximity effect depends on the electronic mean-free path (m.f.p.), l_e , and, thus, on the internal structure. In particular, it has been predicted, that in clean F even a singlet supercurrent should exhibit LRPE [2, 8, 12, 14, 15, 24]. Experimental analysis of SFFS spin-valves has shown that the singlet current is dominant for diluted F [36] and remain considerable even for pure Ni [41]. Clarification of LRPE mechanisms and the ways of controlling supercurrents in S/F heterostructures is important both for fundamental understanding

of unconventional superconductivity [42], and for application in superconducting spintronics [18, 32, 34, 39, 41].

Here we study nanoscale SFS Josephson junctions (JJ's) containing either diluted Ni-alloys $\text{Cu}_{1-x}\text{Ni}_x$ and $\text{Pt}_{1-x}\text{Ni}_x$, Cu/Ni bilayer or pure Ni. Counterintuitively, we observe that the supercurrent density, J_c , through Ni can be much larger than through diluted alloys with the same thickness. Using *in-situ* absolute Josephson fluxometry (AJF), we demonstrate that Ni interlayers in our junctions exhibit full saturation magnetization as in bulk Ni, which precludes presence of extended dead magnetic layers. The clue to understanding of our results is obtained from the analysis of evolution of temperature dependencies, $J_c(T)$, in Nb/ $\text{Pt}_{1-x}\text{Ni}_x$ /Nb JJ's with increasing Ni concentration. It shows that in diluted Ni-alloys, $x \simeq 0.5$, the proximity effect is short range, despite a small E_{ex} , due to an extremely short m.f.p. is such atomically disordered alloys. To the contrary, pure Ni remains clean, facilitating ballistic Cooper pair transport and LRPE similar in scale to that in the normal metal Pt. Our results demonstrate that the proximity effect in ferromagnets depends not only on composition and E_{ex} , but also essentially on the internal structure. This may help to resolve some of the controversies around LRPE. We conclude that strong-but-clean ferromagnets may have advantages compared to weak-but-dirty for device applications.

The paper is organized as follows. In sec. II we describe sample fabrication and experimental procedures. In sec. III we discuss main experimental results, including III A. *in-situ* magnetic characterization of Ni interlayers via AJF and III B. analysis of temperature dependencies of critical currents, which reveals a crossover between clean (ballistic) and dirty (diffusive) transport. In the Appendix we provide additional information about

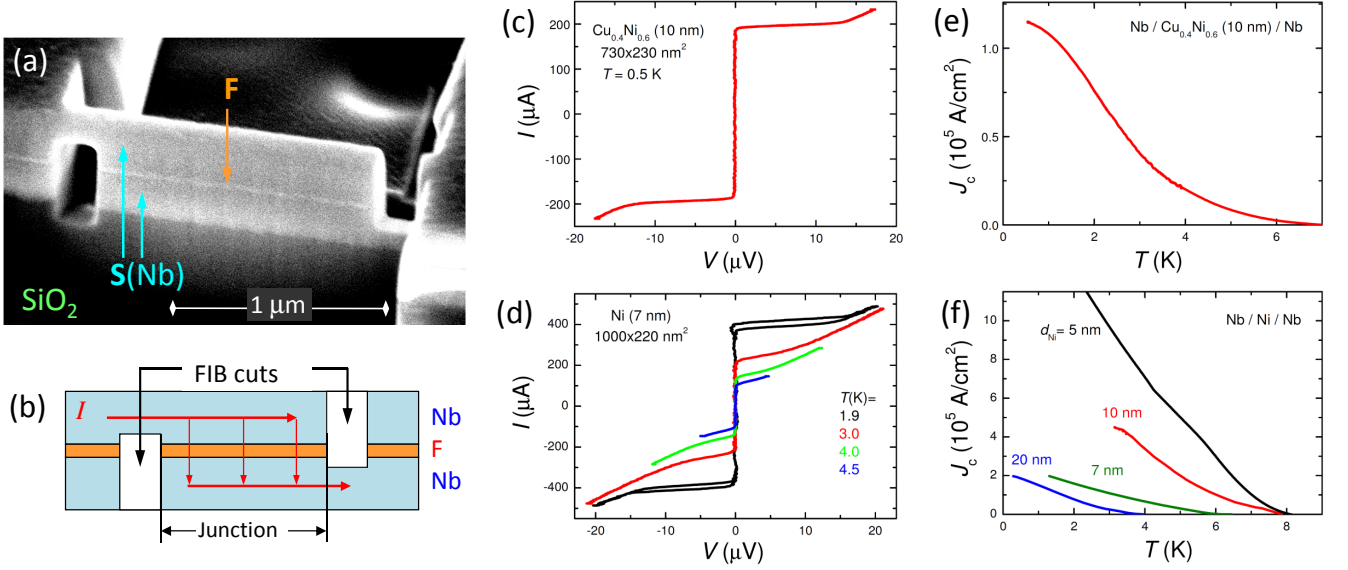


FIG. 1. (color online). (a) SEM image of an SFS junction and (b) a sketch with indication of current flow paths. (c) The I - V curve of Nb/Cu_{0.4}Ni_{0.6}/Nb junction with $d_F = 10$ nm. (d) A set of I - V 's of a Nb/Ni(7 nm)/Nb junction at different T . (e, f) Temperature dependencies of the critical current density for (e) the same Nb/Cu_{0.4}Ni_{0.6}/Nb junction and (f) Nb/Ni/Nb junctions with different Ni thicknesses 5, 7, 10 and 20 nm. Note that the $J_c(T = 3$ K) for the Ni-junction, $d_F = 10$ nm, is almost an order of magnitude larger than that for the junction with diluted Cu_{0.4}Ni_{0.6} interlayer with the same d_F .

A. film structure, B. junction characteristics, C. properties of Nb/Pt_{1-x}Ni_x/Nb junctions, D. interface resistances in Nb/Pt_{1-x}Ni_x/Nb junctions, and E. extraction of magnetization curves from AJF analysis.

II. SAMPLES AND EXPERIMENTAL

We present data for nano-scale SFS junctions with F-interlayers made of Cu_{0.4}Ni_{0.6} and Pt_{1-x}Ni_x alloys with $x = 0 - 1$, pure Ni and a Cu/Ni (N/F, N-normal metal) bilayer. SFS multilayers were deposited by dc-magnetron sputtering in a single cycle without breaking vacuum. Cu_{1-x}Ni_x films were deposited by cosputtering from Cu and Ni targets and the concentration was controlled by the corresponding sputtering rates. Pt_{1-x}Ni_x films were deposited from composite targets with different areas of Ni and Pt segments and Ni concentration was estimated using energy-dispersive X-ray spectroscopy. More details about fabrication and magnetic properties of Pt_{1-x}Ni_x films can be found in Refs. [43, 44] and in Appendices C and D. Nb/Ni/Nb JJ's with different d_F were fabricated from the same wafer with a calibrated Ni-thickness gradient [24]. Nb(S) electrodes were ~ 200 nm thick. Multilayers were first patterned by photolithography and reactive ion etching and then processed by focused ion beam (FIB). Nano-scale JJ's with sizes down to ~ 60 nm were made by FIB-nanosculpturing [26, 36, 45]. Small sizes are necessary both for achieving the monodomain state [41, 46] and for enhancing normal resistances to comfort-

ably measurable values, $R_n \gtrsim 0.1\Omega$. We present data for JJ's with different sizes, interlayer thicknesses, d_F , and compositions. Junction parameters are listed in Tables I-III of the Appendix. Properties of Josephson spin valves with similar CuNi and Ni interlayers can be found in Refs. [36] and [41]. Figure 1 shows (a) a scanning electron microscope (SEM) image of one of the studied Nb/Ni/Nb JJ's and (b) a sketch with a current path.

Measurements are performed in ³He and ⁴He closed-cycle cryostats. Magnetic field, parallel to the junction plane, is supplied by a superconducting solenoid. We will show measurements with field oriented either parallel H_{\parallel} (easy axis), or perpendicular H_{\perp} (hard axis) to the long side of the JJ.

III. RESULTS AND DISCUSSION

Figs. 1 (c,d) show Current-Voltage characteristics (I - V) at zero field for (c) Nb/Cu_{0.4}Ni_{0.6}/Nb junction with $d_F = 10$ nm at $T \simeq 0.5$ K and (d) Nb/Ni/Nb junction with $d_F = 7$ nm at different temperatures, $T = 1.9 - 4.5$ K. The shapes of I - V 's are typical for proximity-coupled JJ's, described by the resistively shunted junction model.

Figs. 1 (e,f) show temperature dependencies of critical current densities for (e) the same Nb/Cu_{0.4}Ni_{0.6}/Nb JJ, and (f) Nb/Ni/Nb JJ's with $d_F = 5, 7, 10$ and 20 nm. It is seen that the JJ with a diluted Cu_{0.4}Ni_{0.6} interlayer has a significantly smaller J_c than the JJ with pure Ni with the same $d_F = 10$ nm, compare red lines in Figs. 1

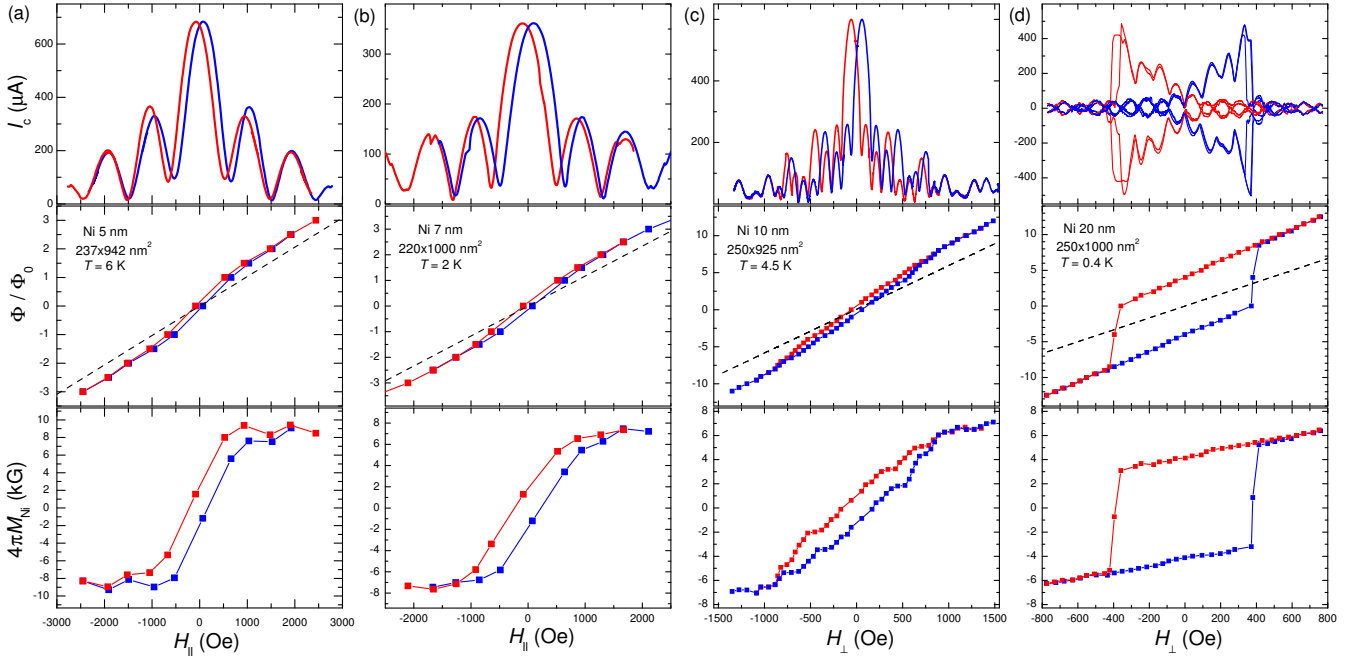


FIG. 2. (color online). Top panels: magnetic field modulation of the critical current, $I_c(H)$, for Nb/Ni/Nb JJ's with d_{Ni} (a) 5 nm and (b) 7 nm in the easy axis orientation and (c) 10 nm and (d) 20 nm in the hard axis orientation. Blue/red lines represent up/down field sweeps. Middle panels show the absolute Josephson fluxometry analysis of the data above. Symbols represent positions of maxima and minima of the $I_c(H)$ patterns, which correspond to half-integer and integer values of Φ/Φ_0 . Bottom panels represent magnetization curves of Ni interlayers obtained from the AJF analysis. Large values of the saturation magnetization $4\pi M_{Ni} \simeq 7$ kG are consistent with the value for bulk Ni and preclude presence of dead magnetic layers.

(e) and (f). It is also seen that the $\text{Cu}_{0.4}\text{Ni}_{0.6}$ JJ exhibits stronger superlinear temperature dependence with a positive curvature $d^2 J_c/dT^2 > 0$ at elevated T , which is well described by the power-law dependence $J_c \propto (1 - T/T_c)^a$ with $a \simeq 3.5$. On the other hand, Ni JJ's show almost linear $J_c(T)$, irrespective of Ni thickness, albeit with a varying onset temperature T_c^* .

III A. *In-situ* magnetic characterization of Ni interlayers via absolute Josephson fluxometry.

Top panels in Figure 2 represent measured $I_c(H)$ modulation patterns for Nb/Ni/Nb JJ's with different d_{Ni} (a) 5 nm, (b) 7 nm, (c) 10 nm and (d) 20 nm. Junction sizes and measurement temperatures are indicated in the Figure. Modulation patterns are shown both for easy (a,b) and hard (c,d) axis orientations. Blue and red lines represent up and down field sweeps. A hysteresis is due to finite coercivity of F-interlayers. It disappears at $H \sim \pm(1 - 1.5)$ kOe, corresponding to transition into the saturated magnetic state. All JJ's, included in the analysis, exhibit Fraunhofer-type $I_c(H)$ modulation, indicating good uniformity of interlayers [47]. Examples of $I_c(H)$ patterns for Nb/PtNi/Nb and Nb/Ni/Nb junctions can be found in Refs. [45] and [41], respectively.

The $I_c(H)$ modulation occurs due to flux quantization.

This can be used for *in-situ* AJF analysis [32, 36, 41], presented in middle panels of Fig. 2. Here symbols represent the flux, $\Phi(H)$, at maxima and minima of $I_c(H)$, which correspond to half-integer and integer number of the flux quantum, Φ_0 , respectively. The total flux is:

$$\Phi = BL\Lambda + 4\pi M_F L d_F, \quad (1)$$

where B is magnetic induction, L is the junction length, Λ is the effective magnetic thickness of the JJ and M_F is magnetization of the F-layer along the field. The first term in the right-hand-side represents the flux induced by magnetic field, the second - by magnetization of the F-layer (for more details see Appendix E).

From Figs. 2 (a,b) it is seen that at large fields $\Phi(H)$ is linear. Since in this case F-layers are in the saturated state, $M_F = M_{sat}$, the linear field dependence is caused solely by the first term in Eq. (1) with $B \propto H$. Subtraction of this linear dependence, shown by dashed lines in middle panels of Fig. 2, reveals the contribution, $\Delta\Phi$, from the second term in Eq. (1). This yields the absolute value of magnetization in the F-interlayer $4\pi M_F = \Delta\Phi/Ld_F$. Thus obtained magnetization curves, $4\pi M_{Ni}(H)$, are shown in bottom panels of Fig. 2. Saturation magnetizations are $4\pi M_{sat} = 8.2 \pm 1.1$ kG for $d_{Ni} = 5$ nm, 7.3 ± 0.5 kG for $d_{Ni} = 7$ nm and 6.9 ± 0.3 kG for $d_{Ni} = 10$ nm. For $d_{Ni} = 20$ nm the saturation magnetization is not reached within the shown field

range (see Appendix E for clarifications). The main uncertainty in M_{sat} is caused by the accuracy of estimation of d_{Ni} , limited by the film roughness $R_q \simeq 1$ nm (see Appendix A). The thinner is the film - the larger is such systematic uncertainty.

The obtained saturation magnetization $4\pi M_{sat} \simeq 7$ kG is consistent with that for bulk nickel [48, 49]. This implies that Ni interlayers in our JJ's are fully ferromagnetic and there are no extended dead magnetic layers, i.e., interface layers of Ni with reduced magnetism. Such dead layers, accompanied by a significant reduction of M_{sat} , were reported in earlier works [23, 26] and would make interpretation of proximity effect more complicated. On the other hand, a variation of the superconducting onset temperature, which can be seen in Figs. 1 (f) and 3 (b), provides an evidence for existence of dead superconducting (rather than magnetic) layers with suppressed T_c^* at junction interfaces.

The large value of M_{sat} confirms that supercurrents in our Nb/Ni/Nb JJ's flow through a pure Ni with strong ferromagnetic properties. Remarkably, we observe a large $J_c \simeq 2 \times 10^5$ A/cm², even through 20 nm of Ni, see Fig. 1 (f). This is a much longer scale compared to earlier reports [21, 26, 27, 31, 34] in which supercurrent was observed only through few nm of Ni. Observation and clarification of such a profound LRPE through a strong F is the main objective of this work.

III B. Temperature dependencies of critical currents: crossover between dirty and clean regimes.

To clarify our observations, we start with a short summary of proximity effects in SNS and SFS JJ's (more detailed analysis can be found in Ref. [50], where various regimes have been considered). In SNS JJ's J_c is determined by the superconducting order parameter at the junction interface, $\Psi_{S/N}$, and the ratio of the thickness, d_N , to the coherence length, ξ_N , of the interlayer. Close to T_c it can be written in the following simple form [51],

$$J_c \propto \Psi_{S/N}^2 \exp\left(-\frac{d_N}{\xi_N}\right). \quad (2)$$

For JJ's with thick d_N , or short ξ_N , $d_N \gg \xi_N(T_c)$, the $J_c(T)$ is determined predominantly by the T -dependence of $\xi_N(T)$, leading to a strong superlinear T -dependence. In the opposite case, $d_N \ll \xi_N(T_c)$, $J_c(T)$ is determined by $\Psi_{S/N}(T)$, leading to a conventional linear $J_c(T)$ close to T_c and a saturation at $T \rightarrow 0$.

For SFS JJ's the coherence length ξ_F is complex [6, 20],

$$\xi_F^{-1} = \xi_{F1}^{-1} + i\xi_{F2}^{-1}. \quad (3)$$

The real part, ξ_{F1} , represents the decay length, the imag-

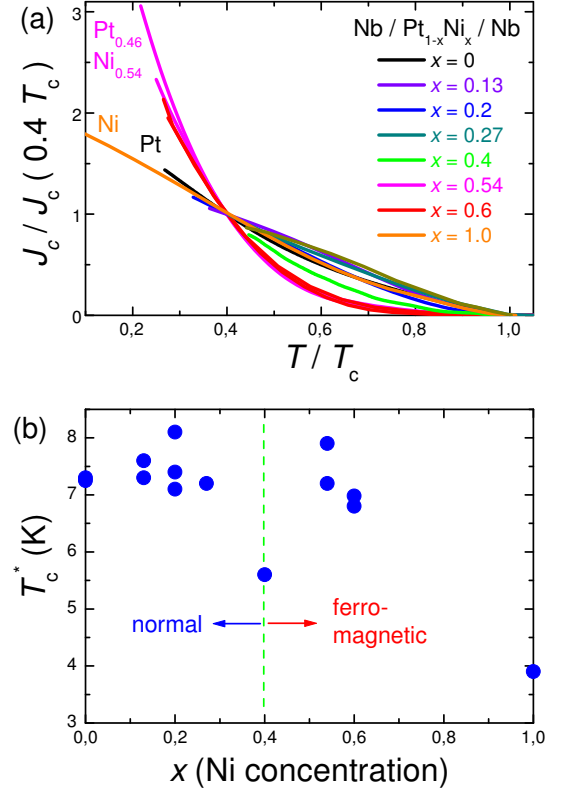


FIG. 3. (color online). (a) Temperature dependencies $J_c(T)$ of Nb/Pt_{1-x}Ni_x/Nb junctions with $d_F = 20$ nm, normalized to the value at $T = 0.4$ of the onset temperature. A gradual evolution of $J_c(T)$ dependencies from linear for pure Pt, $x = 0$, to superlinear at $x \simeq 0.5-0.6$ and back to linear for pure Ni, $x = 1$, indicates a transitions between SNS to dirty SFS and to clean SFS cases. (b) Corresponding onset temperatures of the junctions versus Ni concentration.

inary, $\pi\xi_{F2}$, the period of oscillations. In the clean case,

$$\xi_F(c) = \frac{\hbar v_f}{2(\pi k_B T + iE_{ex})}, \quad (4)$$

where v_f is the Fermi velocity in F. In the dirty case,

$$\xi_F(d) = \sqrt{\frac{l_e}{3}} \xi_F(c). \quad (5)$$

Since here $l_e \ll |\xi_F(c)|$, the coherence length in the dirty case is shorter than in the clean case. For strong F with $E_{ex}/k_B \gg T_c$, in the dirty case $\xi_{F1}(d) \simeq \xi_{F2}(d) \simeq (\hbar l_e v_f / 3E_{ex})^{1/2}$ are equally short. However, in the clean case the two scales are different: $\xi_{F1}(c) \simeq (\hbar v_f / 2\pi k_B T)$, is as long as ξ_N , and $\xi_{F2}(c) \simeq (\hbar v_f / 2E_{ex})$ is short [8, 14, 15, 24]. From the discussion above, it follows that the shape of $J_c(T)$ provides an important clue about the proximity effect [20, 22, 23, 26].

Figure 3 (a) shows evolution of $J_c(T)$, normalized to the value at $0.4T_c^*$ for Nb/Pt_{1-x}Ni_x/Nb JJ's with different Ni concentrations and $d_F \simeq 20$ nm. The onset

temperature T_c^* is shown in Fig. 3 (b). Ferromagnetism in $\text{Pt}_{1-x}\text{Ni}_x$ appears at a critical concentration $x_c = 0.4$ [43, 44], as described in the Appendix C. In Fig. 3 (b), apart from a minimum of T_c^* for the pure Ni, $x = 1$, we can also see a clear minimum at $x_c = 0.4$. Both minima can be interpreted as being due to suppression of $\Psi_{S/N}$ at the interface (dead superconducting layer) due to either a reverse magnetic proximity effect for pure Ni, $x = 1$, or quantum fluctuations at the quantum critical point, $x_c = 0.4$ [44].

From Fig. 3 (a) it can be seen that for a pure Pt, $x = 0$ (black line), $J_c(T)$ is almost linear. As explained above, this is expected for SNS JJ's with $\xi_N(T_c) \gg d_N$. Upon increasing Ni concentration, $J_c(T)$ remains linear for non-magnetic interlayers $x = 0.13, 0.2, 0.27$. At the critical concentration, $x_c = 0.4$ (green line), a positive curvature develops in $J_c(T)$. It becomes most pronounced for $x = 0.5 - 0.6$ (magenta and red curves). Such a transformation is the consequence of a rapid reduction of ξ_F both due to enhancement of E_{ex} and reduction of l_e . While E_{ex} increases linearly at $x > x_c$, the m.f.p. reaches minimum at $x \simeq 0.5$, corresponding to atomically disordered, $l_e \sim 1$ nm, [14] dirty metal (see Appendix C). With further increase of concentration to pure Ni, $x = 1$ (orange line), the linear $J_c(T)$ dependence is restored, similar to a pure Pt, $x = 0$. Such a recovery implies that ξ_{F1} in pure Ni is similarly long as ξ_N for pure Pt, despite the large $E_{ex} \sim 10^3$ K. As discussed above, this indicates occurrence of clean, ballistic transport in Ni. Thus, variation of the shape of $J_c(T)$ reveals two crossovers in electron transport regimes with changing Ni-concentration. First a crossover takes place from a clean SNS type proximity effect in pure Pt to dirty SFS case in diluted, atomically disordered alloy $x \simeq 0.5$. With further increase of x a second crossover from dirty to clean ballistic transport takes place for JJ's with pure Ni.

As mentioned in the Introduction, interpretation of LRPE in strong ferromagnets is still controversial. In several cases it was attributed to appearance of the unconventional odd-frequency spin-triplet order parameter. Recently the dominant ($\sim 70\%$) spin-triplet supercurrent was reported in $\text{SF}_1\text{F}_2\text{S}$ Josephson spin-valve structures with similar Ni-interlayers [41]. However, the triplet supercurrent appears only in the noncollinear state of the spin valve and is tuned by the relative orientation of magnetization in the two F-layers. Appearance and disappearance of the long-range triplet supercurrent upon remagnetization of the spin-valve leads to a profound distortion of the $I_c(H)$ pattern [41]. Such a distortion is the main fingerprint of the triplet component [46] and, thus, provides the key evidence for its existence. SFS junctions, containing just a single F-layer, behave completely differently (see e.g. the discussion in sec. IV C of Ref. [41]). In particular, $I_c(H)$ patterns of all our junctions are Fraunhofer-like, with the only distortion caused by the hysteresis in $M_F(H)$. As discussed in the Introduc-

tion, the triplet state is not anticipated in SFS junctions because there is no obvious mechanism for appearance of the noncollinear magnetic state in the perpendicular direction across the single F-layer. Therefore, we want to emphasize, that LRPE in Nb/Ni/Nb JJ's with clean Ni is achieved by the spin-singlet current without involvement of the unconventional odd-frequency spin-triplet order parameter. Such LRPE is simply a consequence of the lack of scattering mechanism that can destroy singlet Cooper pair correlations in a clean metal (no matter F or N) at $T = 0$ [12]. Thus, it is the cleanliness of pure Ni that facilitates LRPE in Nb/Ni/Nb JJ's. Concurrently, the extreme dirtiness suppresses proximity effect through diluted F-alloys, despite a small E_{ex} .

We also studied Nb/Cu(10nm)/Ni(10nm)/Nb JJ's, with Cu/Ni bilayer. Interestingly, they show an order of magnitude smaller J_c than Nb/Ni(10nm)/Nb JJ's, see Table I in the Appendix, consistent with earlier results for Ni-based JJ's with Cu buffer layers [27, 31, 34]. This is surprising because, due to a large $\xi_N \sim 1 \mu\text{m}$ of Cu, 10 nm should have little influence. On the other hand, neighbors in the periodic table Cu and Ni tend to easily alloy with each other. Therefore, Cu/Ni bilayers likely contain a dirty CuNi interlayer, which leads to suppression of J_c .

CONCLUSIONS

To conclude, we have studied SFS junctions with different Ni-based interlayers. We observed that supercurrents through pure Ni may be much larger than through diluted alloys with much smaller E_{ex} . Analysis of $J_c(T)$ dependencies revealed that this counterintuitive result is caused by the dirtiness of disordered Ni-alloys, leading to a short coherence lengths $\xi_{F1} \sim 1$ nm. To the contrary, the mean-free-path in pure Ni interlayers can easily exceed the film thickness [70] up to several tens of nm, facilitating ballistic Cooper pair transport with the decay length as long as in non-magnetic normal metals. Our observation suggests that SFS junctions with strong-but-clean ferromagnets may have significant advantages, compared to commonly considered weak-but-dirty alloys.

Our results may also help to resolve the controversy around LRPE in strong ferromagnets, which is either seen [19, 30, 35] or not [21, 40]. We want to emphasize that proximity effect in ferromagnets essentially depends on the internal structure. In contrast to SNS JJ's, which always show LRPE at low enough temperatures because $\xi_N(T \rightarrow 0) \rightarrow \infty$ irrespective of cleanliness, for SFS JJ's LRPE occurs only in the clean case, for which $\xi_{F1}(c) \rightarrow \infty$ at $T \rightarrow 0$, while for the dirty case $\xi_{F1}(d)$ remains short irrespective of T . This leads to a principle difference in the range of proximity effects for clean and dirty ferromagnets with otherwise similar compositions and exchange energies.

The work was supported by the EU H2020-WIDESPREAD-05-2017-Twinning project “SPIN-TECH”, grant agreement Nr. 810144 (sample preparation and measurements) and the Russian Science Foundation grant No. 19-19-00594 (data analysis and manuscript preparation). The manuscript was written during a sabbatical semester of V.M.K. at MIPT, supported by the Faculty of Natural Sciences at SU.

Appendix A. Nb/Ni film structure

Figure 4 shows topography maps obtained by atomic force microscopy for (a) a Nb film with thickness $d = 100$ nm and (b-d) Nb/Ni bilayers with increasing Ni thickness. It can be seen that the Nb film has a rise-seed-like structure with elongated crystallites (a). In Nb/Ni bilayers, with increasing Ni thickness, d_{Ni} , the structure of Ni first inherits that of Nb (b) but at $d_{Ni} \simeq 5$ nm a reconstruction to square-shaped crystallites occurs (c), which do not change significantly in shape and size (~ 20 nm) with further increase of d_{Ni} (in the studied range). The mean-square-root roughness of all films is $R_q \simeq 1$ nm, although few spikes up to $\sim \pm 4$ nm can be seen in all cases. Probably because of that, we could not obtain reliable data for junctions with $d_{Ni} < 5$ nm, which were usually shorted and did not exhibit JJ behavior. As can be seen from Fig. 4, the overall roughness of the junction S/F interface is determined by the roughness of the bottom Nb layer and is $R_q \simeq 1$ nm for all studied JJ's.

Appendix B. Summary of junction characteristics

Tables I-III represent characteristics of all types of studied junctions. Figure 5 summarizes measured critical current densities at $T = 3$ K for JJ's with different interlayer composition and thickness, studied in this work. J_c decreases both with increasing Ni concentration and interlayer thickness. For Nb/Ni/Nb JJ's (blue) we have sufficient samples to observe the non-monotonous dependence J_c vs. d_F due to $0 - \pi$ transitions [20, 22, 23, 26]. The blue line, connecting points for Ni-JJ's, however, is drawn solely for the easiness of identification of the data points and does not reflect the anticipated $J_c(d_F)$ dependence, which should oscillate at a much shorter scale $\xi_{F2}(Ni) \sim 1$ nm [26].

Our conclusions are based on the overall analysis of SFS junctions, as listed in Tables I and III. In particular we want to note that the small J_c value for Ni(20nm) JJ in Fig. 5 is the consequence of the much lower onset temperature $T^* < 4$ K for this JJ, as shown in Fig. 3 (b). The data in Fig. 5 is shown for $T = 3$ K. This temperature was chosen because we have data for this T for all junctions. The low T^* of Ni-JJ results in the misleadingly low $J_c(3K)$, as can be seen from Fig. 1

(f). More appropriate comparison should be done for $T \ll T^*$. Such data is listed in Tables I and III and is consistent with our conclusion. One should also keep in mind the oscillatory dependence of J_c on d_F with a nm-scale period of oscillations. Since the periods are different for different ferromagnets, it becomes impossible to make a conclusion by comparing just two JJ's with a fixed d_F . For the same reason we do not claim that J_c in Ni is always larger than in an alloy (which can not be true due to different oscillatory dependencies of the two). Also, because of that we can not make an estimation of decay lengths for our SFS junction. Somewhat reliable decay length estimation from the data in Fig. 5 could be made only for non-magnetic alloys with $x < 0.4$ (see e.g. black and violet lines in Fig. 5 and Table-II) because such JJ's should not exhibit oscillations.

Appendix C. Properties of Nb/Pt_{1-x}Ni_x/Nb junctions

Group-10 elements Pt and Ni are well intermixed with each other and can form solid solutions at arbitrary proportions [52–54]. PtNi alloys should be fairly uniform, contrary to CuNi alloys which are prone to phase segregation and formation of Ni clusters. Therefore, we have chosen this alloy for detailed analysis of variation of properties of SFS junction with the strength of F-interlayer. For that we made a series of Nb/Pt_{1-x}Ni_x/Nb JJ's with different Ni concentrations $x = 0 - 1$. Composition of Pt_{1-x}Ni_x films was estimated using energy-dispersive X-ray spectroscopy [43].

Figures 6 (a) and (b) summarize magnetic properties of thin Pt_{1-x}Ni_x films (35-45 nm thick) obtained in earlier works [43, 44]. Fig. 6 (a) shows the anomalous Hall effect (AHE) conductivity σ_{xy} at the T - x phase diagram. The AHE indicates appearance of the ferromagnetic state [55]. Fig. 6 (b) shows the Curie temperature extracted from Hall measurements. It is seen that ferromagnetism in Pt_{1-x}Ni_x thin films appears at $x > 0.4$, similar to bulk alloys [53].

Pt_{1-x}Ni_x alloys may form a disordered fcc state ($A1$), which is presumably dominant in our sputtered films. However there are also three ordered states Pt₃Ni ($L1_2$), PtNi ($L1_0$) and Ni₃Pt ($L1_2$) with centra of stability at $x = 0.25, 0.5$ and 0.75 , respectively [52, 54]. The most remarkable feature of the AHE in PtNi films, Fig. 6 (a), is the sign-change of σ_{xy} from electron-like to hole-like at $x \simeq 0.4 - 0.6$, which coincides with the expected range of stability of the layered $L1_0$ PtNi compound [52, 54, 56].

Fig. 6 (c) represents residual longitudinal resistivities of the films at $T = 2$ K. The ρ_{xx0} increases upon mixing of Ni and Pt with maximum around $x \simeq 0.5$. This indicates a progressive shortening of the electronic m.f.p. due to the growing disorder. The 50-50 mixture has almost an order of magnitude larger ρ_{xx0} than the pure Ni film

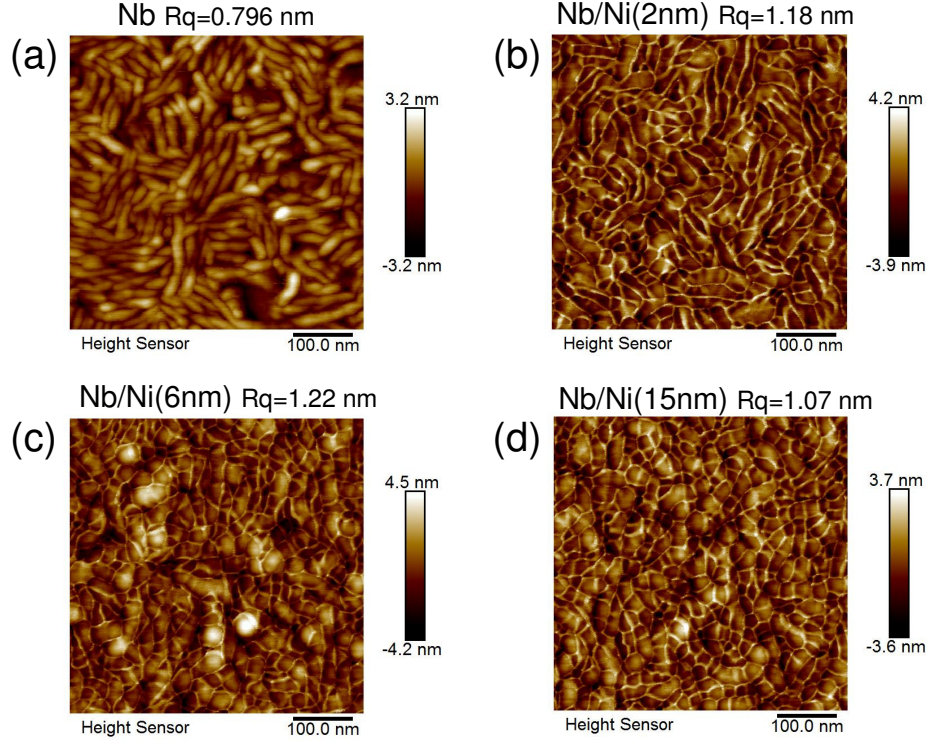


FIG. 4. (color online). Atomic force microscope topography maps of a 100 nm thick Nb film (a) without Ni on top, and (b) with 2 nm Ni, (c) 6 nm Ni and (d) 15 nm Ni films on top. It can be seen that the Ni film reconstruction occurs at about 5 nm thickness.

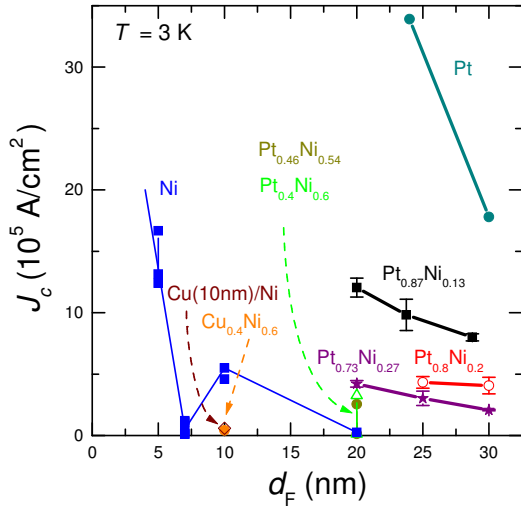


FIG. 5. (color online). A summary of measured critical current densities for different junctions at $T = 3$ K versus the interlayer thickness.

$x = 1$. Simultaneously we also see sharp peaks at $x \simeq 0.4$ and 0.6 , which indicates that additional frustrations in the film structure appears at the borders between stability regions of the ordered $L1_2$ and $L1_0$ states.

Since ferromagnetism in $\text{Pt}_{1-x}\text{Ni}_x$ alloy appears at $x_c \simeq 0.4$, diluted ferromagnets with small $T_{\text{Curie}} \sim 10$ K, comparable to T_c of Nb, correspond to an extremely dirty metallic state. The short electronic m.f.p. leads to a short ξ_F , which leads to a rapid suppression of the proximity induced superconducting order parameter with increasing d_F [6, 15]. Therefore, as discussed in the manuscript, SFS junctions with weak disordered ferromagnets may have small critical current densities despite small exchange fields.

Nb/ $\text{Pt}_{1-x}\text{Ni}_x$ /Nb junctions with different x and d_F were fabricated and studied, see Table II. An example of $I_c(H)$ modulation for Nb/PtNi/Nb JJ can be found in Fig. 4 of Ref. [45]. Figure 7 (a) shows measured $J_c(T = 3\text{K})$ for Nb/ $\text{Pt}_{1-x}\text{Ni}_x$ /Nb junctions versus Ni concentration and interlayer thickness. Fig. 7 (b) shows projection of this data to the J_c - x plane. Generally, J_c decreases both with increasing x and d_F . However, it decreases non-monotonously. Oscillatory decay of J_c vs. d_F in SFS junctions is well documented and is caused by sequential 0 - π transitions [20, 22, 23, 26].

From Fig. 7 it can be seen that for a given d_F the J_c is decaying non-monotonously with increasing Ni concentration x , as indicated by dashed red lines in Fig. 7 (a) for $d_F = 20$ and 30 nm. We attribute such oscillatory behavior to 0 - π transitions at a given d_F upon increasing

TABLE I. Parameters of junctions with Ni, Cu/Ni and CuNi interlayers: d_F is the thickness of F-interlayer; the size defines junction area $A = L_x \times L_y$; R_n is the normal resistance of the junction; $\rho_n = R_n A / d$ is junction resistivity, for junctions with Cu/Ni bilayer $d = d_{Cu} + d_{Ni} = 20$ nm, for the rest $d = d_F$; T is the temperature; I_c is the maximum critical current, $J_c = I_c / A$ is the critical current density; $I_c R_n$ is the characteristic voltage. For some junctions values of I_c , J_c and $I_c R_n$ at different T are provided.

Interlayer	d_F (nm)	Size (nm ²)	R_n (m Ω)	$R_n A$ (10 ⁻¹⁰ Ω cm ²)	ρ_n (10 ⁻⁴ Ω cm)	T (K)	I_c (μ A)	J_c (10 ⁴ (A/cm ²))	$I_c R_n$ (μ V)
Ni	5	855 \times 160	46.8	0.64	1.28	6.2	378	27.7	17.7
Ni	5	942 \times 237	28.3	0.632	1.26	5.2	1110	49.7	31.4
Ni	5	896 \times 164	31	0.456	0.911	3	2800	124	86.8
						5.5	760	51.7	23.6
Ni	7	1100 \times 220	39.9	0.966	1.38	2	30	1.24	1.2
Ni	7	1380 \times 220	21.7	0.66	0.943	2	67	2.21	1.45
Ni	7	950 \times 300	32	0.912	1.3	3.5	100	3.51	3.2
Ni	7	750 \times 220	68	1.12	1.6	2	262	15.88	17.8
Ni	7	1000 \times 220	46	1.01	1.44	3	240	10.9	11.04
Ni	10	865 \times 165	52	0.742	0.742	5.8	324	22.7	16.8
Ni	10	926 \times 250	30.5	0.706	0.706	6.5	311	13.4	9.5
Ni	10	925 \times 250	29	0.671	0.671	4.5	600	26	17.4
						2	1800	77.8	52.2
Cu(10 nm)/Ni	10	800 \times 275	31.5	0.693	0.347	0.49	100	4.55	3.15
Cu(10 nm)/Ni	10	250 \times 200	158	0.79	0.395	0.5	8.5	1.7	1.34
Cu(10 nm)/Ni	10	700 \times 160	53	0.594	0.297	1.8	13.4	1.2	0.71
Cu(10 nm)/Ni	10	700 \times 300	29.15	0.612	0.306	1.8	215	10.2	6.29
Cu(10 nm)/Ni	10	814 \times 250	33	0.6716	0.3358	2.86	95	4.67	3.14
Cu(10 nm)/Ni	10	650 \times 250	47.5	0.772	0.386	0.37	57.5	3.54	2.73
Cu(10 nm)/Ni	10	800 \times 175	53	0.742	0.371	0.37	180	12.86	9.54
Cu _{0.4} Ni _{0.6}	10	730 \times 230	83.5	1.41	1.41	0.56	195	11.6	16.19
Ni	20	1000 \times 250	14	0.35	0.175	0.4	500	20	7.0

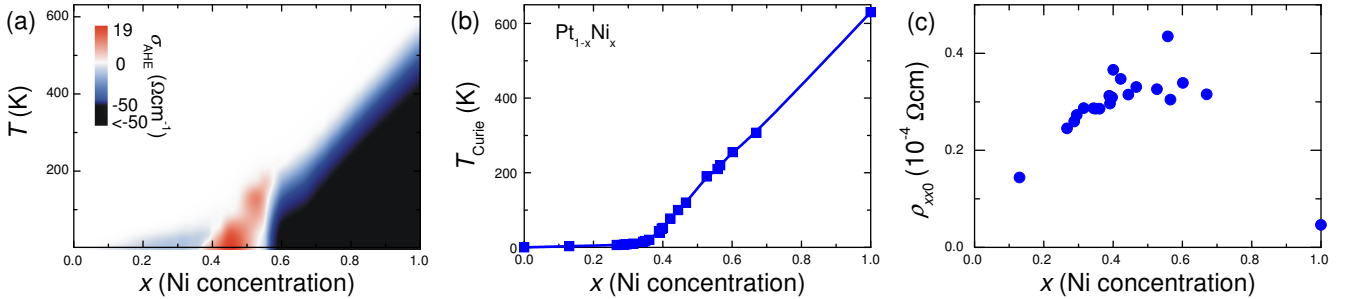


FIG. 6. (color online). Characteristics of $Pt_{1-x}Ni_x$ thin films. (a) Anomalous Hall effect conductivity versus temperature and Ni concentration. (b) Curie temperature obtained from the AHE data. Note that the magnetic quantum phase transition with $T_{Curie} \simeq 0$ occurs at $x_c \simeq 0.4$. (c) Residual in-plane resistivity of films. Maxima of ρ_{xx} are observed at $x \simeq 0.4$ and 0.6 , corresponding to the sign-reversal points of the AHE in panel (a). Data from Refs. [43, 44].

the ferromagnetic exchange energy E_{ex} . The increase of Ni concentration leads to the enhancement of E_{ex} , which leads to the shrinking of ξ_F and cause the $0-\pi$ transition. As described above, ferromagnetism in $Pt_{1-x}Ni_x$ films appears at the critical concentration $x_c \simeq 0.4$. We observe that the relative spread in J_c values increases

in JJ's with the ferromagnetic interlayer $x > 0.4$. Most likely this is also a consequence of a rapid shrinkage of ξ_F down to about 1 nm, comparable to the roughness of our films, see Fig. 4.

TABLE II. Parameters of junctions with Pt and paramagnetic PtNi interlayers.

Interlayer	d_F (nm)	Size (nm ²)	R_n (m Ω)	$R_n A$ (10 ⁻¹⁰ Ω cm ²)	ρ_n (10 ⁻⁴ Ω cm)	T (K)	I_c (μ A)	J_c (10 ⁴ A/cm ²)	$I_c R_n$ (μ V)
Pt	23.75	207 \times 104	340	0.732	0.31	1.8	1400	651	476
						3.2	762	354	259
Pt	23.75	274 \times 113	220	0.68	0.287	1.8	1700	548	374
Pt	25	180 \times 90	680	1.1	0.44	2.5	160	98.7	108.8
Pt	30	106 \times 106	710	0.8	0.27	3.2	200	178.6	142
Pt	30	170 \times 88	500	0.75	0.25	3.2	260	173.3	130
Pt	30	117 \times 88	780	0.8	0.27	3.2	156	151.5	121.7
Pt _{0.87} Ni _{0.13}	20	351 \times 85	270	0.806	0.402	3.0	180	60.4	67.2
Pt _{0.87} Ni _{0.13}	20	308 \times 128	160	0.631	0.315	3.1	430	109	68.8
Pt _{0.87} Ni _{0.13}	20	330 \times 139	133	0.61	0.305	3.1	570	124	75.8
Pt _{0.87} Ni _{0.13}	20	372 \times 130	125	0.605	0.303	3.2	610	126	76.3
Pt _{0.87} Ni _{0.13}	20	340 \times 122	138	0.572	0.286	3.2	510	122.9	70.4
Pt _{0.87} Ni _{0.13}	23.75	226 \times 222	146	0.733	0.38	3.0	460	91.7	67.2
Pt _{0.87} Ni _{0.13}	23.75	228 \times 175	187	0.746	0.314	3.0	360	90.2	67.3
Pt _{0.87} Ni _{0.13}	23.75	235 \times 192	133	0.60	0.253	3.0	510	113	67.8
Pt _{0.87} Ni _{0.13}	28.75	237 \times 134	190	0.603	0.21	2.8	240	76	45.6
Pt _{0.87} Ni _{0.13}	28.75	218 \times 180	210	0.824	0.286	2.8	300	76.5	63
Pt _{0.87} Ni _{0.13}	30	110 \times 100	1180	1.298	0.432	2.76	28	25.4	33.0
Pt _{0.87} Ni _{0.13}	30	140 \times 120	660	1.109	0.37	2.7	65	38.7	42.9
Pt _{0.8} Ni _{0.2}	20	197 \times 144	180	0.511	0.255	2.9	230	81.3	41.4
Pt _{0.8} Ni _{0.2}	20	229 \times 144	210	0.693	0.345	2.9	300	91.2	63
Pt _{0.8} Ni _{0.2}	25	287 \times 106	302	0.919	0.367	3.0	120	39.5	36.2
Pt _{0.8} Ni _{0.2}	25	277 \times 128	248	0.879	0.352	3.0	155	43.7	38.4
Pt _{0.8} Ni _{0.2}	25	170 \times 106	462	0.833	0.333	3.0	80	44.4	37
Pt _{0.8} Ni _{0.2}	25	287 \times 106	307	0.934	0.373	3.0	125	41.1	38.4
Pt _{0.8} Ni _{0.2}	25	319 \times 64	390	0.796	0.318	3.0	80	39.2	31.2
Pt _{0.8} Ni _{0.2}	30	319 \times 106	237	0.801	0.267	3.1	120	35.5	28.4
Pt _{0.8} Ni _{0.2}	30	266 \times 128	228	0.776	0.258	3.1	130	38.2	29.6
Pt _{0.8} Ni _{0.2}	30	319 \times 117	181	0.676	0.225	3.1	180	48.3	32.6
Pt _{0.73} Ni _{0.27}	20	210 \times 120	415	1.046	0.523	3.2	101.5	40.3	42.1
Pt _{0.73} Ni _{0.27}	20	210 \times 170	293	1.046	0.523	3.2	157	44	46
Pt _{0.73} Ni _{0.27}	20	212 \times 90	530	1.011	0.506	3.2	72	37.7	38.2
Pt _{0.73} Ni _{0.27}	20	210 \times 190	245	0.978	0.489	3.2	179	44.9	43.9
Pt _{0.73} Ni _{0.27}	20	202 \times 140	360	1.02	0.509	3.2	120	42.4	43.2
Pt _{0.73} Ni _{0.27}	20	180 \times 175	335	1.05	0.528	3.2	137	43.5	45.9
Pt _{0.73} Ni _{0.27}	20	175 \times 140	300	0.735	0.368	3.2	130	53.1	39
Pt _{0.73} Ni _{0.27}	20	255 \times 96	320	0.783	0.392	3.2	136	55.5	43.5
Pt _{0.73} Ni _{0.27}	25	158 \times 149	375	0.883	0.353	3.1	61.5	26.2	23.1
Pt _{0.73} Ni _{0.27}	25	175 \times 123	330	0.71	0.284	3.1	74	34.4	24.4
Pt _{0.73} Ni _{0.27}	30	266 \times 193	203	1.04	0.347	3.1	104	20.3	23.9
Pt _{0.73} Ni _{0.27}	30	266 \times 167	218	0.968	0.323	3.1	95	21.4	20.7
Pt _{0.73} Ni _{0.27}	30	256 \times 140	278	0.996	0.332	3.1	73	20.4	20.3

Appendix D. Interface resistances in Nb/Pt_{1-x}Ni_x/Nb junctions

Figure 8 (a) shows a 3D plot of measured normal resistivities, ρ_n , of studied Nb/Pt_{1-x}Ni_x/Nb junctions versus

Ni concentration and interlayer thickness. Parameters of JJ's are listed in Table III. Here $\rho_n = R_n A / d_F$, where A is the junction area. Fig. 8 (b) shows the 2D projection of same data. It is seen that ρ_n greatly increases at

TABLE III. Parameters of junctions with ferromagnetic PtNi interlayers.

Interlayer	d_F (nm)	Size (nm ²)	R_n (m Ω)	$R_n A$ (10 ⁻¹⁰ Ω cm ²)	ρ_n (10 ⁻⁴ Ω cm)	T (K)	I_c (μ A)	J_c (10 ⁴ (A/cm ²))	$I_c R_n$ (μ V)
Pt _{0.6} Ni _{0.4}	25	630 \times 230	50	0.725	0.29	2.2	160	11	8
Pt _{0.6} Ni _{0.4}	25	770 \times 320	50	1.23	0.493	2.2	63	2.6	3.2
Pt _{0.6} Ni _{0.4}	25	770 \times 320	220	5.42	2.17	2.2	2070	84	455*
Pt _{0.6} Ni _{0.4}	30	300 \times 165	2000	9.9	3.3	3.0	140	28.3	280*
Pt _{0.6} Ni _{0.4}	30	380 \times 180	1030	5.19	1.73	3.0	7.5	1.5	7.7
Pt _{0.6} Ni _{0.4}	30	260 \times 110	2200	6.29	2.09	3.0	18.3	6.4	40.3
Pt _{0.6} Ni _{0.4}	30	640 \times 225	120	1.73	0.58	3.3	0	0	0
Pt _{0.6} Ni _{0.4}	30	640 \times 225	300	4.32	1.44	2.8	110	7.6	33
Pt _{0.46} Ni _{0.54}	20	800 \times 225	50	0.9	0.45	1.8	63	3.5	3.2
						3.0	28	1.56	1.4
Pt _{0.46} Ni _{0.54}	20	1140 \times 230	120	3.15	1.57	1.8	2100	80	252*
						3.0	800	30.5	96
Pt _{0.46} Ni _{0.54}	20	1140 \times 380	22	0.95	0.477	1.8	92	2.1	2.0
Pt _{0.4} Ni _{0.6}	20	1200 \times 300	90	3.24	1.62	1.8	3490	96.9	314.1*
						3.0	1480	41.2	133.2
Pt _{0.4} Ni _{0.6}	20	1050 \times 420	25	1.1	0.55	1.8	136	3.08	3.4
						3.0	62	1.41	1.6
Pt _{0.4} Ni _{0.6}	25	630 \times 340	51	1.09	0.44	0.4	81	3.8	4.1
Pt _{0.4} Ni _{0.6}	25	640 \times 340	53	1.15	0.46	0.4	73	3.4	3.9
Pt _{0.4} Ni _{0.6}	25	670 \times 310	53	1.10	0.44	0.4	58	2.8	3.1
Pt _{0.4} Ni _{0.6}	25	510 \times 310	73	1.16	0.46	0.4	73	4.6	5.3
Pt _{0.4} Ni _{0.6}	25	550 \times 330	71	1.29	0.52	0.4	91	5.0	6.5
Pt _{0.4} Ni _{0.6}	25	460 \times 300	86	1.19	0.47	0.4	110	8.0	9.5
Pt _{0.4} Ni _{0.6}	25	560 \times 310	69	1.2	0.48	0.4	49	2.8	3.4
Pt _{0.33} Ni _{0.67}	20	350 \times 190	160	1.064	0.53	2.0	0	0	0
Pt _{0.33} Ni _{0.67}	20	350 \times 120	260	1.092	0.55	2.0	0	0	0
Pt _{0.33} Ni _{0.67}	20	290 \times 182	200	1.056	0.53	2.0	0	0	0
Pt _{0.33} Ni _{0.67}	20	410 \times 180	160	1.18	0.59	2.0	0	0	0
Pt _{0.33} Ni _{0.67}	20	490 \times 160	130	1.02	0.51	2.0	0	0	0
Ni	20	1000 \times 250	14	0.35	0.175	0.4	500	20	7.0
						2.0	188	7.5	2.6
						3.0	57	2.3	0.8

* The very large $I_c R_n$ values are not confident because the corresponding large I_c is comparable to the onset of the flux-flow phenomenon in Nb electrodes. This leads to the non-linear I - V 's at large bias and makes it difficult to correctly estimate R_n .

$x = 0.4 - 0.6$ which is correlated with the region with maximal longitudinal resistance of PtNi films, see Fig. 6 (c). Thus frustration and disorder is directly reflected in junction characteristics. However, ρ_n exhibits a much larger peaks at the frustration points $x \simeq 0.4$ and 0.6 , compared to ρ_{xx0} . Especially at the onset of ferromagnetism $x_c = 0.4$, where ρ_n increases by almost an order of magnitude. This indicates that properties of SFS junctions depend not only on the electronic disorder (m.f.p.) but also on the magnetic disorder and, particularly, are affected by quantum fluctuations at the quantum phase transition reflected by the sign-change of the AHE, Fig. 6 (a).

From the comparison of ρ_{xx0} and ρ_n , Figs. 6 (c) and 8 (b) it is also seen that junction resistivity is several times larger than the film resistivity. This indicates that junction resistances are dominated by an additional resistance at S/F interfaces due to a finite interface transparency $\beta < 1$. For SNS junctions the interface transparency is reduced by a mismatch between Fermi velocities and Fermi surfaces (electronic band structures) of S and N metals [57, 58]. For example, the transparency of Nb/Cu interface was estimated to be $\beta \simeq 0.4$ [57]. The transparency of S/F interfaces is further reduced due to spin imbalance, which affects the Andreev reflection of spin-singlet Cooper pairs from spin-polarized ferromag-

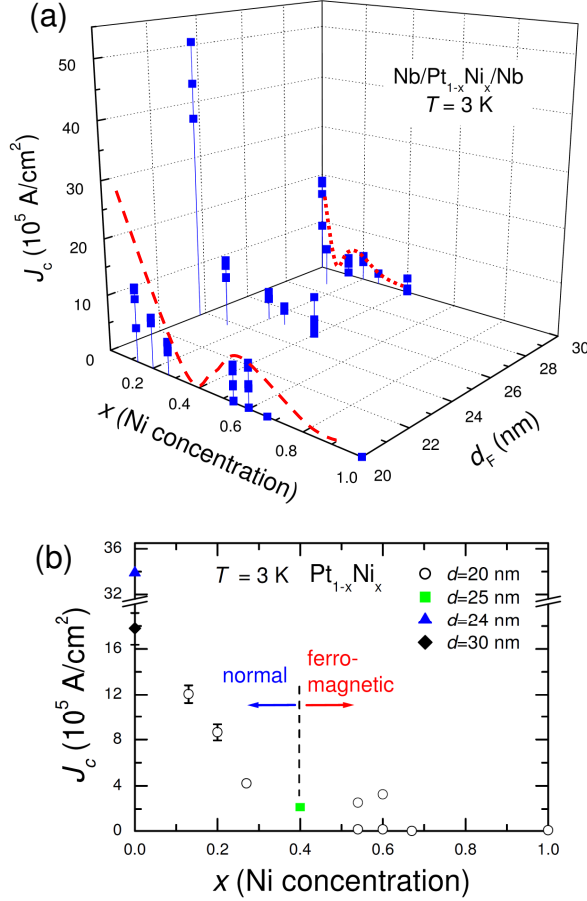


FIG. 7. (color online). (a) Three-dimensional plot of critical current densities of Nb/Pt_{1-x}Ni_x/Nb junctions at $T = 3 \text{ K}$ as a function of Ni concentration and interlayer thickness. (b) Projection of the same data to the two-dimensional plot. Red dashed lines in (a) indicate possible $0-\pi$ transition for a fixed d_F upon increasing Ni concentration.

net [1, 4, 58–64]. The values $R_n A \sim 1 \times 10^{-10} \Omega \text{cm}^2$ in our junctions, see Tables I–III, are comparable to the value $0.64 \times 10^{-10} \Omega \text{cm}^2$ reported for Nb/Co interfaces [64]. From Table III it can be seen that for Nb/Pt_{1-x}Ni_x/Nb JJ's with $x \simeq 0.4$ and 0.6 , corresponding to quantum critical points of vanishing AHE, $\sigma_{AHE}(T = 0) \simeq 0$, see Fig. 6 (a) and Ref. [44], the $R_n A$ value and, thus, the interface resistance greatly increases. Simultaneously the critical current density increases, leading to extraordinary large $I_c R_n$ products of several hundreds of μV , comparable to that for SINIS (I-insulator) junctions [65]. The origin of this phenomenon remains to be understood. So far we can only speculate that anomalous junction characteristics at these critical concentrations are related to quantum phase transitions occurring between ordered $L1_0$ and $L1_2$ phases with different magnetic properties [52, 54, 56, 66]. For all our junctions, R_n is dominated by S/F interface resistances, consistent with earlier reports

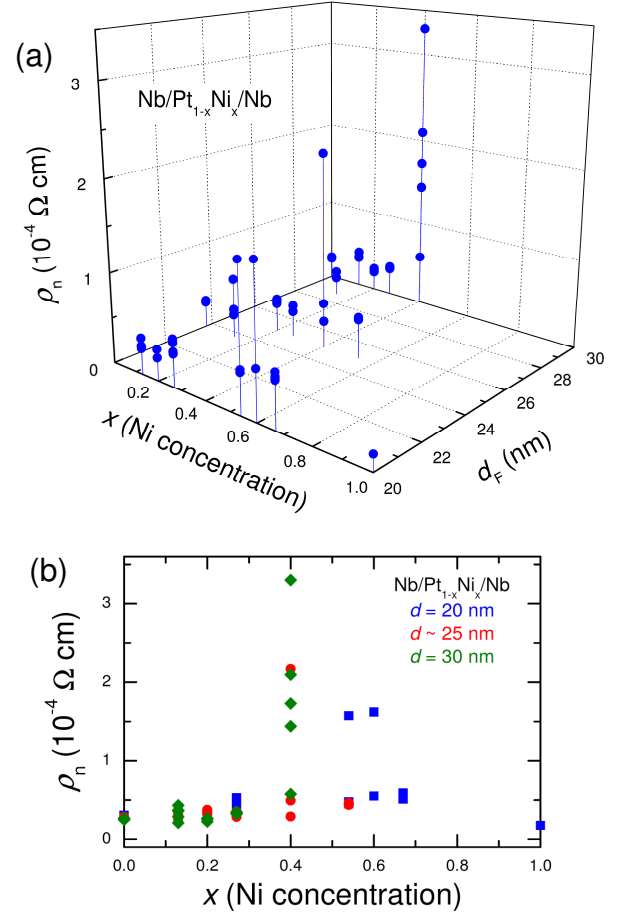


FIG. 8. (color online). (a) Three-dimensional plot of normal resistivities of Nb/Pt_{1-x}Ni_x/Nb junctions versus Ni concentration and interlayer thickness. (b) Projection of the same data on the two-dimensional plot. Note sharp singularities at the critical concentration $x_c = 0.4$ and a secondary maximum at $x \simeq 0.6$, corresponding to points of sign-reversal AHE in Fig. S3 (a).

for other types of S/F interfaces [58, 62, 64]. Therefore, there are significant barriers at S/F interfaces, despite the deposition of SFS trilayers occurred in one run without breaking vacuum.

Appendix E. Clarification about extraction of magnetization curves from AJF analysis

In derivation of Eq. (1) we assumed that M_F has an in-plane orientation. Due to the small thickness of F-interlayers, they have negligibly small demagnetization factors. In this case the F-layer does not generate magnetic fields at S/F interfaces and, therefore, does not induce any additional flux in S-electrodes. This leads to a simple separation of flux contributions from S-electrodes and F-interlayer, represented by first and second terms

in Eq. (1). Here B in the first term does not contain M_F (i.e it is not $H + 4\pi M_F$) and differs from H solely due to screening by superconducting currents and a finite demagnetization factor of S-electrodes, just like in the non-magnetic junction. Since for our junctions the total thickness of S-layers $2d_{Nb} = 400$ nm is comparable to junction sizes, the demagnetization factor of electrodes is non-negligible and the difference between B and H can be sensible. Nevertheless, this does not affect the linearity of $\Phi(H)$ curves above the saturation field because $B \propto H$ in the presence of the demagnetization effect. Therefore, subtraction of the linear asymptotics, shown by dashed lines in middle panels of Fig. 2 (a-c), remains unambiguous.

The distance between points in the AJF analysis is determined by the flux quantization field $\Delta H = \Phi_0/L\Lambda$. It is smaller for the hard axis orientation of the field, corresponding to the longest size of the junction L . Therefore, AJF curves for the hard axis, Figs. 2 (c,d), are much more detailed than for the easy axis orientation, Figs. 2 (a,b). Nevertheless, extraction of $M_F(H)$ for the hard axis orientation is complicated by two factors: First, magnetization reversal in the hard axis orientation occurs initially via coherent rotation of magnetization (without hysteresis), followed by a small flip, and continuing coherent rotation towards the saturated state [41, 46, 67, 68]. Since the flip is smaller than M_{sat} , it does not allow direct extraction of M_{sat} from the size of the magnetization jump. Second, since the length of the electrode $L \sim 1 \mu\text{m}$ in the hard axis orientation is much larger than the London penetration depth of S-electrodes, $\lambda_S \simeq 100$ nm, junctions are prone to penetration of Abrikosov vortices, which greatly distort junction characteristics [45, 69]. Therefore, the field range of our analysis is limited by the range of the Meissner state.

For the JJ with $d_{Ni} = 10$ nm, Fig. 2 (c), the Meissner state persists up to the saturation state and the straightforward subtraction of the high-field linear slope from the AJF curves, shown by the dashed line in the middle panel of Fig. 2 (c), provides a magnetization loop with the expected saturation at high fields, as shown in the bottom panel of Fig. 2 (c). It can be seen that saturation occurs at $H \simeq 1$ kOe, which is consistent with that obtained using the first-order reversal curves analysis on the same junction, see Fig. 2 (f) in Ref. [41].

For the JJ with $d_{Ni} = 20$ nm, Fig. 2 (d), the field range is limited by entrance of Abrikosov vortices. It is smaller than 1 kOe and the saturation is presumably not reached, which does not allow unambiguous determination of the linear asymptotics. In this case we have chosen to assume $B = H$ in Eq. (1) and calculate the first linear term using the definition of the magnetic thickness, $\Lambda = d_F + \lambda_{S1} \tanh(d_{S1}/2\lambda_{S1}) + \lambda_{S2} \tanh(d_{S2}/2\lambda_{S2})$, where $d_{S1,2} = 200$ nm are the thicknesses and $\lambda_{S1,2} = 100$ nm are the London penetration depths of the two Nb-electrodes. The corresponding linear dependence $\Phi_1(H)$

is shown by the dashed line in the middle panel of Fig. 2 (d). Thus obtained magnetization curve, $M_{Ni}(H_\perp)$, shown in the bottom panel of Fig. 2 (d), is in line with the expected magnetization curve for the hard axis orientation, as discussed above, and provides a correct value of M_{sat} .

* E-mail: Vladimir.Krasnov@fysik.su.se

- [1] M. J. M. de Jong and C. W. J. Beenakker, Andreev Reflection in Ferromagnet-Superconductor Junctions, *Phys. Rev. Lett.* **74**, 1657 (1995).
- [2] E.A. Demler, G.B. Arnold, M.R. Beasley, Superconducting proximity effects in magnetic metals, *Phys. Rev. B* **55**, 15174 (1997).
- [3] A. Kadigrobov, R. I. Shekhter and M. Jonson, Quantum spin fluctuations as a source of long-range proximity effects in diffusive ferromagnet-superconductor structures. *Europhys. Lett.* **54**, 394 (2001).
- [4] B. P. Vodopyanov, and L. R. Tagirov, Andreev Conductance of a Ferromagnet/Superconductor Point Contact, *JETP Lett.* **77**, 126-131 (2003).
- [5] J. Kopu, M. Eschrig, J. C. Cuevas, and M. Fogelström, Transfer-matrix description of heterostructures involving superconductors and ferromagnets. *Phys. Rev. B* **69**, 094501 (2004).
- [6] A. I. Buzdin, Proximity effects in superconductor-ferromagnet heterostructures. *Rev. Mod. Phys.* **77**, 935-976 (2005).
- [7] F. S. Bergeret, A. F. Volkov, and K. B. Efetov, Odd triplet superconductivity and related phenomena in superconductor-ferromagnet structures. *Rev. Mod. Phys.* **77**, 1321-1373 (2005).
- [8] M. Božović and Z. Radović, Ferromagnet-superconductor proximity effect: The clean limit, *Europhys. Lett.* **70**, 5137519 (2005). DOI: 10.1209/epl/i2004-10511-0
- [9] Y. Asano, Y. Sawa, Y. Tanaka, and A.A. Golubov, Odd triplet superconductivity and related phenomena in superconductor-ferromagnet structures. *Phys. Rev. B* **76**, 224525 (2007).
- [10] M. A. Silaev, Possibility of a long-range proximity effect in a ferromagnetic nanoparticle. *Phys. Rev. B* **79**, 184505 (2009).
- [11] Ya. V. Fominov, A. A. Golubov, T. Yu. Karminskaya, M. Yu. Kupriyanov, R. G. Deminov, and L. R. Tagirov, Superconducting Triplet Spin Valve. *JETP Lett.* **91**, 308 (2010).
- [12] F. Konschelle, J. Cayssol and A. Buzdin, Long-range singlet proximity effect in ferromagnetic nanowires, *Phys. Rev. B* **82**, 180509(R) (2010).
- [13] M. Alidoust, J. Linder, G. Rashedi, T. Yokoyama, and A. Sudbø, Spin-polarized Josephson current in superconductor/ferromagnet/superconductor junctions with inhomogeneous magnetization, *Phys. Rev. B* **81**, 014512 (2010).
- [14] N. G. Pugach, M. Yu. Kupriyanov, E. Goldobin, R. Kleiner, and D. Koelle, Superconductor-insulator-ferromagnet-superconductor Josephson junction: From the dirty to the clean limit, *Phys. Rev. B* **84**, 144513 (2011).
- [15] A.S. Mel'nikov, A.V. Samokhvalov, S.M. Kuznetsova, and A.I. Buzdin, Interference Phenomena and Long-

- Range Proximity Effect in Clean Superconductor-Ferromagnet Systems. *Phys. Rev. Lett.* **109**, 237006 (2012).
- [16] S. H. Jacobsen and J. Linder, Giant triplet proximity effect in π -biased Josephson junctions with spin-orbit coupling, *Phys. Rev. B* **92**, 024501 (2015).
- [17] I. V. Bobkova, A. M. Bobkov, and M. A. Silaev, Gauge theory of the long-range proximity effect and spontaneous currents in superconducting heterostructures with strong ferromagnets, *Phys. Rev. B* **96**, 094506 (2017).
- [18] N. Klenov, Y. Khaydukov, S. Bakurskiy, R. Morari, I. Soloviev, V. Boian, T. Keller, M. Kupriyanov, A. Sidorenko, and B. Keimer, Periodic Co/Nb pseudo spin valve for cryogenic memory, *Beilstein J. Nanotechnol.* **10**, 833-839 (2019). doi:10.3762/bjnano.10.83
- [19] V. T. Petrashov, I. A. Sosnin, I. Cox, A. Parsons, and C. Troadec, Giant Mutual Proximity Effects in Ferromagnetic/Superconducting Nanostructures, *Phys. Rev. Lett.* **83**, 3281 (1999).
- [20] V. V. Ryazanov, V. A. Oboznov, A. Yu. Rusanov, A. V. Veretennikov, A. A. Golubov, and J. Aarts, Coupling of Two Superconductors through a Ferromagnet: Evidence for a π Junction, *Phys. Rev. Lett.* **86**, 2427 (2001).
- [21] J. Aumentado and V. Chandrasekhar, Mesoscopic ferromagnet-superconductor junctions and the proximity effect, *Phys. Rev. B* **64**, 054505 (2001).
- [22] T. Kontos, M. Aprili, J. Lesueur, F. Genêt, B. Stephanidis, and R. Boursier, Josephson Junction through a Thin Ferromagnetic Layer: Negative Coupling, *Phys. Rev. Lett.* **89**, 137007 (2002).
- [23] V. A. Oboznov, V. V. Bol'ginov, A. K. Feofanov, V. V. Ryazanov, and A. I. Buzdin, Thickness Dependence of the Josephson Ground States of Superconductor-Ferromagnet-Superconductor Junctions, *Phys. Rev. Lett.* **96**, 197003 (2006).
- [24] F. Born, M. Siegel, E. K. Hollmann, H. Braak, A. A. Golubov, D. Yu. Gusakova and M. Yu. Kupriyanov, Multiple $0 - \pi$ transitions in superconductor/insulator/ferromagnet/superconductor Josephson tunnel junctions, *Phys. Rev. B* **74**, 140501(R) (2006).
- [25] R. S. Keizer, S. T. B. Goennenwein, T. M. Klapwijk, G. Miao, G. Xiao, and A. Gupta, A spin triplet supercurrent through the half-metallic ferromagnet CrO_2 , *Nature (London)* **439**, 825 (2006).
- [26] J. W. A. Robinson, S. Piano, G. Burnell, C. Bell, and M. G. Blamire, Zero to π transition in superconductor-ferromagnet-superconductor junctions, *Phys. Rev. B* **76**, 094522 (2007).
- [27] A. A. Bannykh, J. Pfeiffer, V. S. Stolyarov, I. E. Batov, V. V. Ryazanov, and M. Weides, Josephson tunnel junctions with a strong ferromagnetic interlayer, *Phys. Rev. B* **79**, 054501 (2009).
- [28] J. W. A. Robinson, G. B. Halász, A. I. Buzdin, and M. G. Blamire, Enhanced Supercurrents in Josephson Junctions Containing Nonparallel Ferromagnetic Domains, *Phys. Rev. Lett.* **104**, 207001 (2010).
- [29] M. Flokstra, J. M. van der Knaap, and J. Aarts, Magnetic coupling in superconducting spin valves with strong ferromagnets. *Phys. Rev. B* **82**, 184523 (2010).
- [30] J. Wang, M. Singh, M. Tian, N. Kumar, B. Liu, C. Shi, J. K. Jain, N. Samarth, T. E. Mallouk, and M. H. W. Chan, Interplay between superconductivity and ferromagnetism in crystalline nanowires, *Nat. Phys.* **6**, 389 (2010).
- [31] K. M. Boden, W. P. Pratt Jr., and N. O. Birge, Proximity-induced density-of-states oscillations in a superconductor/strong-ferromagnet system, *Phys. Rev. B* **84**, 020510(R) (2011).
- [32] V. V. Bol'ginov, V. S. Stolyarov, D. S. Sobanin, A. L. Karpovich, and V. V. Ryazanov, Magnetic Switches Based on NbPdFeNb Josephson Junctions with a Magnetically Soft Ferromagnetic Interlayer *JETP Lett.* **95**, 366-371 (2012).
- [33] T. Golod, A. Rydh, V. M. Krasnov, I. Marozau, M. A. Uribe-Laverde, D. K. Satapathy, Th. Wagner, and C. Bernhard, High bias anomaly in $\text{YBa}_2\text{Cu}_3\text{O}_{7-x}/\text{LaMnO}_{3+\delta}/\text{YBa}_2\text{Cu}_3\text{O}_{7-x}$ superconductor/ferromagnetic insulator/superconductor junctions: Evidence for a long-range superconducting proximity effect through the conduction band of a ferromagnetic insulator, *Phys. Rev. B* **87**, 134520 (2013).
- [34] B. Baek, W. H. Rippard, S. P. Benz, S. E. Russek, and P. D. Dresselhaus Hybrid superconducting-magnetic memory device using competing order parameters *Nat. Commun.* **5**, 3888 (2014).
- [35] M. Kompaniets, O. V. Dobrovolskiy, C. Neetzel, E. Begun, F. Porrati, W. Ensinger, and M. Huth, Proximity-induced superconductivity in crystalline Cu and Co nanowires and nanogranular Co structures. *J. App. Phys.* **116**, 073906 (2014).
- [36] A. Iovan, T. Golod, and V. M. Krasnov, Controllable generation of a spin-triplet supercurrent in a Josephson spin valve, *Phys. Rev. B* **90**, 134514 (2014).
- [37] D. Lenk, V. I. Zdravkov, J.-M. Kehrle, G. Obermeier, A. Ullrich, R. Morari, H.-A. Krug von Nidda, C. Müller, M. Yu. Kupriyanov, A. S. Sidorenko, S. Horn, R. G. Deminov, L. R. Tagirov and R. Tidecks, Thickness dependence of the triplet spin-valve effect in superconductor-ferromagnet-ferromagnet heterostructures. *Beilstein J. Nanotechnol.* **7**, 957 (2016).
- [38] K. Lahabi, M. Amundsen, J. A. Ouassou, E. Beukers, M. Pleijster, J. Linder, P. Alkemade, and J. Aarts. Controlling supercurrents and their spatial distribution in ferromagnets. *Nature Commun.* **8**, 2056 (2017).
- [39] N. O. Birge, Spin-triplet supercurrents in Josephson junctions containing strong ferromagnetic materials, *Phil. Trans. R. Soc. A* **376**, 20150150 (2018). <http://dx.doi.org/10.1098/rsta.2015.0150>
- [40] O. V. Skryabina, S. N. Kozlov, S. V. Egorov, A. A. Klimenko, V. V. Ryazanov, S. V. Bakurskiy, M. Yu. Kupriyanov, N. V. Klenov, I. I. Soloviev, A. A. Golubov, K. S. Napolskii, I. A. Golovchanskiy, D. Roditchev and V. S. Stolyarov, Anomalous magneto-resistance of Ni-nanowire/Nb hybrid system, *Sc. Rep.* **9**, 14470 (2019). <https://doi.org/10.1038/s41598-019-50966-8>
- [41] O. M. Kapran, A. Iovan, T. Golod, and V. M. Krasnov, Observation of the dominant spin-triplet supercurrent in Josephson spin valves with strong Ni ferromagnets. *Phys. Rev. Research* **2**, 013167 (2020).
- [42] J. Linder and A. V. Balatsky, Odd-frequency superconductivity. *Rev. Mod. Phys.* **91**, 045005 (2019).
- [43] T. Golod, A. Rydh and V. M. Krasnov, Anomalous Hall effect in NiPt thin films, *J. Appl. Phys.* **110**, 033909 (2011).
- [44] T. Golod, A. Rydh, P. Svedlindh and V. M. Krasnov, Anti-ordinary Hall effect near the ferromagnetic quantum phase transition in $\text{Ni}_x\text{Pt}_{1-x}$ thin films, *Phys. Rev. B* **87**, 104407 (2013).
- [45] T. Golod, A. Rydh, and V. M. Krasnov, Detection of the Phase Shift from a Single Abrikosov Vortex. *Phys. Rev.*

- Lett.* **104**, 227003 (2010).
- [46] A. Iovan and V. M. Krasnov, Signatures of the spin-triplet current in a Josephson spin valve: A micromagnetic analysis. *Phys. Rev. B* **96**, 014511 (2017).
 - [47] V.M. Krasnov, V.A. Oboznov, and N.F. Pedersen, Fluxon dynamics in long Josephson junctions in the presence of a temperature gradient or spatial nonuniformity, *Phys. Rev. B* **55**, 14486-14498 (1997).
 - [48] A. T. Aldred, Temperature dependence of the magnetization of nickel, *Phys. Rev. B* **11**, 2597 (1975).
 - [49] H. Danan, A. Herr, and A. J. P. Meyer, New Determinations of the Saturation Magnetization of Nickel and Iron, *J. Appl. Phys.* **39**, 669 (1968); DOI: <https://doi.org/10.1063/1.2163571>.
 - [50] A. A. Golubov, M. Yu. Kupriyanov, and E. Il'ichev, The current-phase relation in Josephson junctions, Review of Modern Physics **76**, 411-469 (2004).
 - [51] A. A. Golubov and V. M. Krasnov, The first critical field, H_{c1}^{\perp} , and the penetration depth in dirty superconducting S/N multilayers, *Physica C* **196**, 177-184 (1992).
 - [52] C. E. Dahmani, M. C. Cadeville, J. M. Sanchez, and J. L. Moran-Lopez, Ni-Pt Phase Diagram: Experiment and Theory, *Phys. Rev. Lett.* **55**, 1208 (1985).
 - [53] M. J. Besnus and A. Herr, Transition from ferromagnetism to paramagnetism in Ni-Pt alloys, *Phys. Lett. A* **39**, 83 (1972).
 - [54] A. Hizi, H. Garbouj, C. Mottet, M. Said, Chemical ordering and surface segregation in $\text{Ni}_{1-c}\text{Pt}_c$ system: A theoretical study from the alloys to the nanoalloys, *Results in Physics* **14**, 102493 (2019).
 - [55] N. Nagaosa, J. Sinova, S. Onoda, A. H. MacDonald, and N. P. Ong, Anomalous Hall effect, *Rev. Mod. Phys.* **82**, 1539 (2010).
 - [56] H. Zhang, S. Blügel, and Yu. Mokrousov, Anisotropic intrinsic anomalous Hall effect in ordered 3dPt alloys, *Phys. Rev. B* **84**, 024401 (2011).
 - [57] V. M. Krasnov, V. A. Oboznov and V. V. Ryazanov, Anomalous temperature dependence of H_{c1}^{\perp} in superconducting Nb/Cu multilayer, *Physica C* **196**, 335-339 (1992).
 - [58] S. K. Upadhyay, A. Palanisami, R. N. Louie, and R. A. Buhrman, Probing Ferromagnets with Andreev Reflection, *Phys. Rev. Lett.* **81**, 3247 (1998).
 - [59] J. Aarts, J. M. E. Geers, E. Brück, A. A. Golubov, and R. Coehoorn, Interface transparency of superconductor/ferromagnetic multilayers, *Phys. Rev. B* **56**, 2779 (1997).
 - [60] V. I. Fal'ko and C. J. Lambert, and A. F. Volkov, Andreev reflections and magnetoresistance in ferromagnet/superconductor mesoscopic structures, *JETP Lett.* **69**, 532 (1999).
 - [61] A. A. Golubov, Interface resistance in ferromagnet-superconductor junctions, *Physica C* **326-327**, 46-52 (1999).
 - [62] O. Bourgeois, P. Gandit, A. Sulpice, J. Lesueur and X. Grison, Transport in superconductor/ferromagnet/superconductor junctions dominated by interface resistance, *Phys. Rev. B* **63**, 064517 (2001).
 - [63] K. Xia, P. J. Kelly, G. E. W. Bauer, and I. Turek, Spin-Dependent Transparency of Ferromagnet/Superconductor Interfaces, *Phys. Rev. Lett.* **89**, 166603 (2002).
 - [64] S. F. Lee, S. Y. Huang, J. H. Kuo, Y. A. Lin, L. K. Lin, and Y. D. Yao, Quantitative analysis of interface resistance in Co/Nb multilayers for normal and superconducting Nb, *J. Appl. Phys.* **93**, 8212 (2003).
 - [65] A. A. Golubov, E.P. Houwman, J. G. Gijsbertsen, V. M. Krasnov, J. Flokstra, and H. Rogalla, Proximity effect in superconductor-insulator-superconductor Josephson tunnel junctions: Theory and experiment, *Phys. Rev. B* **51**, 1073 (1995).
 - [66] M. Chen, Z. Shi, W.J. Xu, X.X. Zhang, J. Du, and S.M. Zhou, Tuning anomalous Hall conductivity in L_{10} FePt films by long range chemical ordering, *Appl. Phys. Lett.* **98**, 082503 (2011).
 - [67] Y. Henry, A. Iovan, J.-M. George, and L. Piraux, Statistical analysis of the magnetization processes in arrays of electrodeposited ferromagnetic nanowires, *Phys. Rev. B* **66**, 184430 (2002).
 - [68] Yu. P. Ivanov, O. Iglesias-Freire, E. V. Pustovalov, O. Chubykalo-Fesenko, and A. Asenjo, Magnetic configurations of Co(111) nanostripes with competing shape and crystalline anisotropies, *Phys. Rev. B* **87**, 184410 (2013).
 - [69] T. Golod, A. Pagliero and V. M. Krasnov, Two mechanisms of Josephson phase shift generation by an Abrikosov vortex, *Phys. Rev. B* **100**, 174511 (2019).
 - [70] For in-plane transport the electronic m.f.p. is limited by the film thickness due to interface scattering. However, here we consider perpendicular transport, for which such scattering is irrelevant. Therefore, the effective m.f.p. in the perpendicular direction is not limited by the film thickness.